

Single-Process 3D-Printed Stacked Dielectric Actuator

Tibor Barši Palmić^a, Janko Slavič^{a,*}

^a*University of Ljubljana, Faculty of Mechanical Engineering, Aškerčeva 6, 1000
Ljubljana, Slovenia*

Cite as:

*Tibor Barši Palmić and Janko Slavič, Single-Process 3D-Printed Stacked Dielectric Actuator, International Journal of Mechanical Sciences (2022),
<https://doi.org/10.1016/j.ijmecsci.2022.107555>*

Abstract

Single-process additive manufacturing provides fully functional 3D-printed structures in a single 3D printer without the need for additional manufacturing processes. The 3D-printed parts can be scaled, individualised, embedded, and combined into multi-functional structures without modifications to the fabrication technology.

This manuscript reports the first demonstration of monolithically 3D-printed stacked dielectric actuators (SDEAs) in a single fabrication process utilising a commercially accessible extrusion 3D printer and thermoplastic filaments. Neither single-layer nor stacked dielectric actuators have been 3D printed with thermoplastic filament extrusion in a single process until now.

To achieve single-process fabrication, this research successfully addresses the main challenges: single-process fabrication of the dielectric layer and electrodes, repeatability and reliability of the 3D-printed thin dielectric layer, and layer stacking.

Four actuators with different active areas and a number of stacked active layers were 3D printed. The functionality of the 3D-printed actuators was demonstrated with dynamic electromechanical characterization in a free-displacement and blocked-force configuration in a broad frequency range (up to 5 kHz).

The actuators show promise for applications that require high-frequency

*Corresponding author

Email address: janko.slavic@fs.uni-lj.si (Janko Slavič)

resonators or high controllability in the sub-resonance region.

Keywords: dielectric actuator, fused-filament fabrication, dynamic operation, free displacement characterization, blocked force characterization, smart structures

1. Introduction

Recent contributions to the subject of solid-state actuation describe actuators with diverse functionalities. Actuation mechanisms with faster response, *i.e.*, electrostatic [1, 2], piezoelectric [3, 4], electromagnetic [5, 6, 7], and dielectric [8], were utilised for microbeam [9] and membrane [10] resonators, membrane speakers [11], and fast-switching bistable actuators [12]. Slower actuation mechanisms, *i.e.*, pneumatic [13], thermomechanical [14, 15], phase-change [16] and shape-memory [17] effects, were utilised for biomimetic robots [18], soft grippers [19], artificial muscles [20], and origami self-folding structures [21].

The additive manufacturing of solid-state actuators provides important advantages, *e.g.*, low-cost single-process fabrication, individualization, complex shapes, fast prototyping, and integrated sensing [22, 23]. The recent research drive towards multi-material 3D-printed functional structures (sensors [24, 25, 26, 27], actuators [18, 28, 29], electrical circuits [30, 31], and batteries [32]) are the foundations for future 3D-printed individualised smart structures [33, 34].

The achievable excitation force and response time of 3D-printed actuators are dependent on the underlying actuating mechanism and the material properties. Because of the solid-state design that is necessitated by the actuating mechanisms and 3D printing's limitations, most 3D-printed actuators belong to the field of soft robotics [35], which means relatively low-frequency operation.

Electronic electro-active (dielectric and piezoelectric) actuating mechanisms demonstrate faster responses than pneumatic/hydraulic, thermomechanical, and shape-memory effects. The achievable response time is also restricted by the mechanical properties of the utilised materials; *e.g.*, softer polymers (gels, elastomers) increase the response time and reduce the actuating force because of the pronounced visco-(hyper)elastic effects [36].

Although, the first classically manufactured DEAs were presented decades ago, the field is still developing and expanding with advances in materials and

fabrication technologies towards novel applications [37]. The fast response of DEAs was utilised in vibroacoustic applications like active and passive vibration isolation [10, 38] and noise damping or attenuation (dielectric speakers) [39]. The flexibility of dielectric elastomers makes possible soft robots that are capable of walking [40], swimming [41], and flying [42]. The repeatable response and accuracy of DEAs are utilised, for example, for micro- and nano-positioning systems [43], active lenses [44], haptic feedback [45], and tremor-suppression devices [46]. The dielectric effect makes it possible to have dielectric grippers for object holding without energy consumption (dielectric minimum energy structures - DEMES) [47]. The simple and flexible design was also utilised to produce micro-pumps and fluid-control devices in microfluidics [48], contributing to the fields of biomimetic structures and lab-on-a-chip devices.

The recent development of materials resulted in elastomers with increased permittivity and electric breakdown stability [49, 50] and compliant electrodes fabricated with polymer liquids [51], hydrogels [52], nanomaterials (carbon and metal) [53], and polymer nanocomposites [54]. These new advances in polymers and polymer composites provide extremely flexible electrodes and new fabrication techniques [55]. The assortment of dielectric materials was also expanded from silicon-, acryl- and polyurethane-based elastomers to include liquid and gel-like polymers with self-healing capabilities [56], polymer composites with increased dielectric permittivity [57, 58], and copolymers with improved breakdown stability and prestrained molecular structures (interpenetrating polymer networks) [59].

Most stacked DEAs (SDEAs) are fabricated using manual methods (prefab. foils and films, spin-coating, spray deposition, etc.). Li et al. [60] presented a SDEA fabricated with a circular process of casting and curing of the liquid dielectric, followed by the casting and curing of the electrode material, and stacking of the active layers for the desired number of layers. Kelley et al. [46] developed an SDEA for tremor suppression using a folding method; a three-part silicon was cured and folded into a stacked configuration and carbon powder was manually brushed-on, serving as the electrodes. Rossiter et al. [61] utilised an ink-jet 3D printer for the fabrication of a stiff frame and dielectric layer for an antagonistic annular DEA; the electrodes were applied manually in the form of silver paste. In 2018, Haghiashtiani et al. [62] developed an ionic hydro-gel polymer for the electrodes and a silicon-based dielectric, which were used in a direct ink writing (DIW) process to print a dielectric unimorph actuator. In 2020, Chortos et al. developed

conductive and dielectric ink materials with self-healing properties for DIW. The electrodes and the stiff frame were printed and the dielectric was cast and cured in the printed frame. Quasi-static and dynamic characterizations between 1 and 100 Hz were performed [63]. Gonzalez et al. [64] used a fused-filament-fabrication (FFF) technology and printed a DE layer for a circle membrane actuator with a commercial thermoplastic polyurethane (TPU) filament. Electrodes were applied manually after the printing and the characterization was quasi-static.

FFF 3D-printing technology is based on the extrusion of a thermoplastic polymer that is fed into the machine in filament form [65, 66]. The desired shape of the printed part is sliced into horizontal layers that are sequentially printed onto each other. Each layer is a composition of individually extruded traces of the polymer melt that solidify and form a solid base for the next layers. The main advantages are the accessibility of the machines, the extensive selection of compatible polymers [67] and functional polymer composites [68], and multi-material 3D printing capability [69], all of which make it one of the most widespread polymer 3D-printing technologies.

From the literature review it is clear that in 3D printing the main fabrication challenge is the uneven surface of the printed TPU layer which results, in an electromechanical pull-in instability and frequent dielectric breakdowns. In terms of the accuracy and repeatability of FFF technology, research has to be performed to advance the skills and knowledge for a successful printing strategy to decrease the electromechanical instability and increase the repeatability and performance of the printed DEAs. Furthermore, the methods for relatively high-frequency dynamic characterization of printed DEAs have to be researched.

In this manuscript, FFF technology and commercial filament materials are used to 3D print a SDEA in a single process without manual intervention. A stacked configuration consisting of horizontal interchanging electrodes and dielectric layers is the most suitable for the layer-by-layer deposition process and high-frequency dynamic operation. The printing procedure, including the surfacing of each printed layer, enabled the fabrication of four SDEAs with different active areas and numbers of active layers. The dynamic electromechanical characterization was performed with the devised methods in fixed-free and fixed-fixed configurations, enabling a precise analysis of the dynamic operation and the study of the effects of the actuator's dimensions.

The manuscript is organised as follows. In Sec. 2, the theoretical background of the dielectric effect is presented. Sec. 3 presents the fabrication,

while Sec. 4 and 5 present the electrical and electromechanical characterizations, respectively. The results are given in Sec. 6, while Sec. 7 discusses the results. Finally, last section draws the conclusions.

2. Theoretical background

This section presents the fundamental theoretical background to dielectric actuation. The dielectric electromechanical coupling is presented with the example of a single active layer comprising a dielectric film sandwiched between two opposite electrodes. The example configuration with the latter used coordinate system is shown in Fig.1.

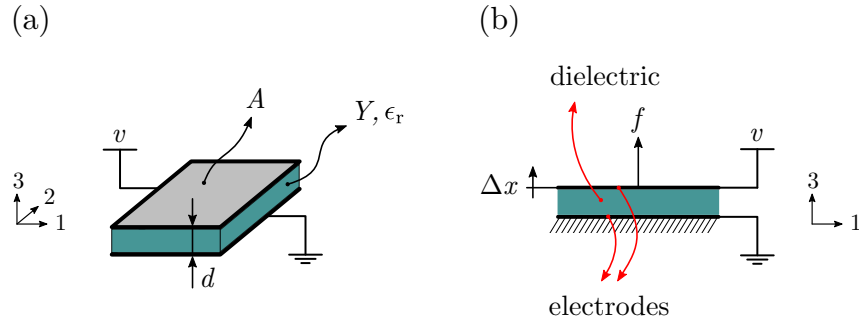


Figure 1: **A simplified example of an active dielectric layer.** (a) 3D view with visible top electrode and electrical connection to a voltage source v , marked dimensions (area A and thickness d), and material properties (elastic modulus Y , relative permittivity ϵ_r) of the dielectric. (b) Side view with marked generated force f and displacement of the top electrode Δx .

The dielectric actuation mechanism using the Maxwell stress approach for the (33)-direction is defined as [70]:

$$T_{33} = \epsilon_r \epsilon_0 E_3^2. \quad (1)$$

The mechanical stress T_{33} generated in the dielectric layer depends on the relative permittivity ϵ_r (ϵ_0 is the permittivity of a vacuum) and the square of the electric field E_3 . The electric field:

$$E = \frac{v}{d} \quad (2)$$

is established with a voltage potential v (applied to the opposite electrodes) and is inversely proportional to the thickness of the dielectric layer d , see

Fig.1.

If the electric field and mechanical stress are uniform, the generated force can be simplified to [71]:

$$f = -\epsilon_r \epsilon_0 A \left(\frac{v}{d} \right)^2, \quad (3)$$

where A is the active area of the actuator. To derive the generated strain S_{33} when the actuator is activated, the elastic modulus Y has to be taken into account. If the electrodes are assumed to be ideally compliant, the strain is defined as [71]:

$$S_{33} = -\epsilon_r \epsilon_0 \left(\frac{v}{d} \right)^2 \frac{1}{Y}. \quad (4)$$

The displacement Δx can be derived from the strain S_{33} :

$$\Delta x = -\epsilon_r \epsilon_0 \frac{v^2}{d} \frac{1}{Y}. \quad (5)$$

The generated displacement Δx is proportional to ϵ_r and v^2 and inversely proportional to d and Y .

3. Fabrication

This section presents the technology and materials, explaining the modifications to the commercial multi-material 3D printer and the fundamental reasoning behind the material selection. Secondly, the design of the actuator is presented and the fabrication method in terms of material extrusion and deposition strategy is described.

3.1. FFF technology and materials

From the theoretical background it is clear that dielectric actuation requires thin (d) and flexible (Y) active layers, which presents technological issues with regards to: 3D printing resolution, minimal achievable thickness, and material selection.

Specifically for FFF technology, resolution in the xy-plane is dependent on the extruded trace width, which is limited by the nozzle diameter. In contrast, the z-axis resolution is dependent only on the z-axis drive resolution, which is about 5 μm for a typical FFF 3D printer. Consequently, thin features are best printed horizontally.

All the actuators were printed on an E3D ToolChanger (E3D-Online, United Kingdom) with four independent direct extruders enabling the fabrication of structures with four different materials. The printer was further modified and retrofitted with an auto-calibration system for the x-, y-, and z-axis and a camera system for visual inspection of the printed layers during and after the print job. These modifications substantially improved the efficiency of the print-fault determination and increased the printing's success rate.

The auto-calibration system enabled the individual calibration of each nozzle offset. It consisted of a piezo switch and a camera mounted on the side of the print bed. The z-axis was calibrated by recording the height of the z-axis at the point of contact between the nozzle and the piezo switch. The x- and y-axis were calibrated with a camera that was vertically mounted towards the nozzle orifice. A circle-fitting algorithm defined the nozzle's offset in the x-y plane. The whole calibration procedure was performed on an external Raspberry Pi computer connected to the printer's control board. The camera system for the visual inspection of the printed layers was mounted on the tool holder. It was also controlled by the Raspberry Pi. It was activated by the g-code at the required layer heights.

The mechanical elasticity of the used materials greatly impacts on the actuating strain, and highly flexible materials for the dielectric and conductive elements are desired. To achieve a higher actuating strain, multiple active layers can be stacked together. SDEAs operating in a longitudinal out-of-plane configuration (shown in Fig. 2), are the focus of this research.

Conventional dielectric materials used for dielectric actuators exhibit exceptional flexibility to achieve large actuating strains. Extrusion of flexible materials with a commercial FFF 3D printer is challenging as the filament must provide sufficient stiffness for the reliable grip with the extruder gears and must resist buckling of the filament before the melting zone. To achieve a reliable dielectric layer the material with the best compromise between flexibility and printability was chosen.

As for the dielectric also the electrodes need to be as flexible as possible to enable the deformation of the active layer. In addition, they must provide sufficient electrical conductivity to charge the dielectric at high voltage amplitudes and frequencies.

The actuators presented in this manuscript were printed with NinjaTek Eel and Trcek TPU. This pair of materials provided the best compromise between printability and flexibility. Also, since both materials are based on

TPU, a good adhesion during and after printing was achieved. NinjaTek Eel provided sufficient conductivity to successfully charge the actuators in the characterization frequency range (up to 5 kHz).

3.2. DEA design and fabrication strategy

The SDEA was composed of three distinct layers, shown in Fig. 2b, that were printed alternately to achieve the desired interdigitated stacked configuration. The dielectric layer comprised of the dielectric in the middle with contacts on the left- and right-hand sides for the left and right electrodes, respectively. Two other distinct layers were comprised of an electrode, a contact for the opposite electrode, and an isolating dielectric segment in-between. The electrode was isolated with a dielectric perimeter to prevent dielectric breakdown on the edge of the actuator (see Fig. 2c).

The main challenges encountered during 3D printing were unevenly printed surfaces, which are a typical consequence of the extrusion-deposition FFF process. Contributing to the unevenness is filament-diameter variation that can result in over-/under-extrusion of the material and pronounced high/low spots in the printed layer. The uneven surface onto which the new material is being deposited can result in inter-layer contamination. One compromised dielectric layer is sufficient to cause electromechanical instability and drastically decrease the dielectric breakdown strength of the whole stacked actuator. Nozzle fouling and stringing can also lead to contaminated layers. Strings of flexible material act as an obstruction, preventing even and uniform material deposition, which is transferred to subsequent layers and can result in an electrical contact between opposite electrodes through the dielectric.

The presented problems were substantially reduced with the development of a custom g-code generation program. The custom program enabled an individual specification of process parameters and deposition strategies for each region (shown in Fig.2) of the printed actuator. The most beneficial extrusion and deposition parameters were: perimeter, infill, and ironing start position, nozzle wipe position, infill and ironing raster angle, extrude rate, and printing speed.

A major improvement in surface quality was achieved with the ironing of each electrode and the dielectric surface. Ironing is a process where a hot nozzle is dragged over the already-printed surface with a narrower path spacing flattening the printed surface to the specified layer height. With ironing, extra material from over-extrusion can be pushed to the side of the

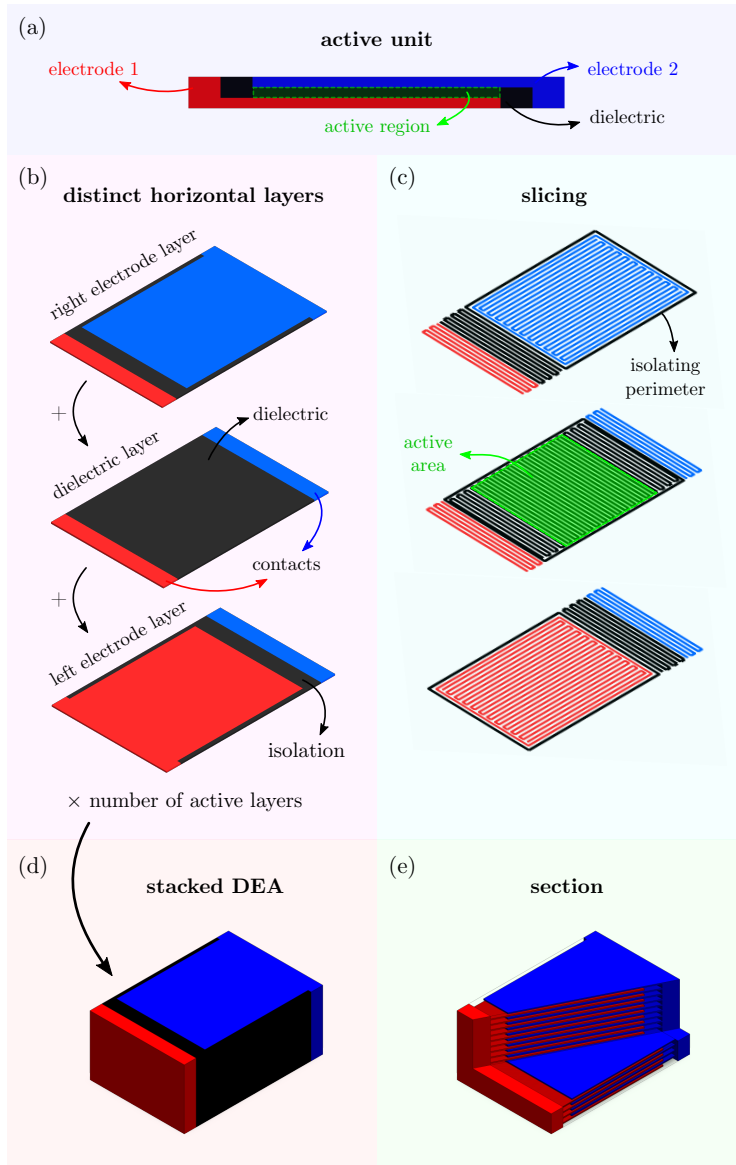


Figure 2: **SDEA design.** (a) Single active unit with the opposing electrodes (red and blue) and the dielectric (black) with marked active region (compressed when active). (b) Three distinct layers of the active unit: two electrode layers with the electrode, contact regions, and isolation regions and a dielectric layer with the dielectric and two contact regions. (c) Sliced layers for extrusion 3D printing with visible individual traces of the extruded material. (d) The individual active units are stacked into a stacked actuator. (e) Section of the stacked actuator with transparent dielectric.

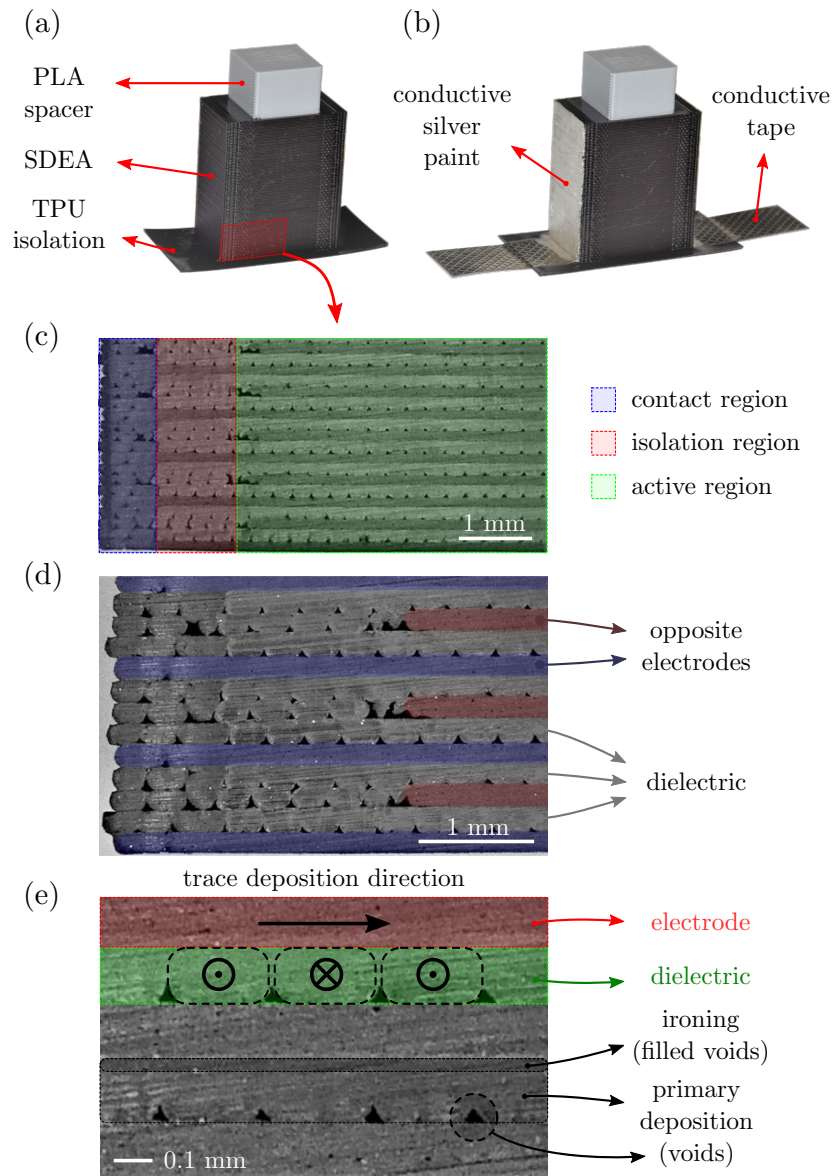


Figure 3: **3D-printed SDEA.** (a) Actuator after printing with electrical isolation on the bottom and PLA spacer on the top. (b) Actuator after the application of conductive tape and silver paint for electrical contacting. (c) Section of the printed actuator with the colored contact (blue), isolation (red), and active (green) regions. (d) Close-up of the contact and isolation region with visible traces of the dielectric and conductive materials and colored opposite electrodes. (e) Close-up of the active region with marked direction of trace deposition of conductive and dielectric materials with the evident void-filling effect of the ironing of each layer.

actuator as long as the starting position and raster angle are appropriately specified.

Electrical contacts between the printed electrodes and the electrical excitation equipment were manually fabricated with a conductive, embossed tin-plated copper foil (3M, part num. 1345) and conductive silver paint (ElectroLube, SCP), as is shown in Fig. 3.

4. Electrical characterization

Electrical characterization was performed using the two-probe impedance measurement of the Digilent Analog Discovery 2 oscilloscope (Digilent Inc., USA) and an impedance-measurement module. The module enabled an impedance measurement with calibrated shunt resistors and compensation for the connecting cables. Electrical impedance, defined as:

$$Z(\omega) = \frac{V(\omega)}{I(\omega)} = R + \frac{1}{j\omega C(\omega)} [\Omega], \quad (6)$$

is comprised of the resistance R and capacitance C of the system. The electrodes and the connecting cables represent the resistance and the dielectric represents the capacitance.

The relative permittivity of the dielectric was calculated from the measured capacitance:

$$\epsilon_r(\omega) = C(\omega) \frac{d}{NA\epsilon_0}, \quad (7)$$

where $C(\omega)$ is the frequency-dependent capacitance and d , N , and A represent the dielectric layer thickness, number of active layers, and active area, respectively.

5. Electromechanical characterization

Electromechanical characterization was performed in a dynamic operational regime. Each actuator was characterised in a fixed-free and fixed-fixed boundary condition where the generated acceleration of the free-end and actuating force were measured, respectively.

Excitation was performed with an A-303 High-Voltage Amplifier (A. A. Lab Systems Ltd., Israel). The excitation voltage was a pure sine wave (AC) without the static component (DC) and was measured with a 100:1 voltage probe and a National Instruments DAQ card.

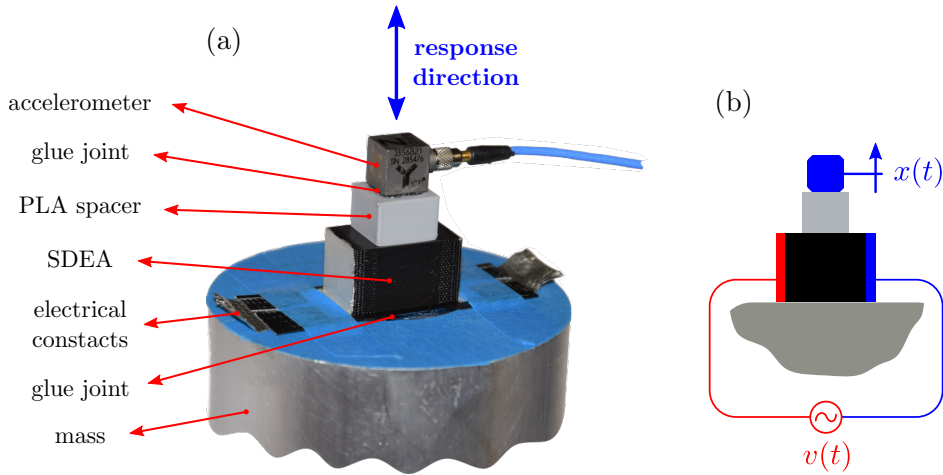


Figure 4: **Experimental setup for dynamic free-displacement characterization.** (a) The actuator is glued onto a vibro-isolated mass and the 3-axis accelerometer is glued onto the printed spacer on top of the actuator with the primary response in the vertical direction. (b) Front view sketch of the characterization setup with the electrical connection $v(t)$ and primary displacement response $x(t)$.

The actuators exhibited a high electrical capacitance, reducing the voltage capability of the amplifier. In the frequency range from 100 Hz to 5 kHz and excitation voltage from 60 V to 130 V, the response of the amplifier was found to be linear. The amplifier was voltage controlled at an amplitude of 60 V to prevent any voltage variation from affecting the dynamic characteristic of the actuator.

Measurements of the excitation voltage and the mechanical response were performed at discrete frequencies with a step of 10 Hz. The excitation frequency range was 100 Hz to 2.5 kHz and 100 Hz to 1 kHz for the free-displacement and blocked-force characterizations, respectively. Since the dielectric effect exhibits quadratic electromechanical coupling and the excitation voltage was a pure sine wave, the actuators responded with a doubled excitation frequency. For that reason, the frequency-response characteristics were defined by the Fourier transform of a squared voltage-time signal.

5.1. Free-displacement characterization

Fixed-free or free-displacement characterization enables the analysis of an actuator in a no-load condition. The frequency response of an actuator, therefore, includes only the unobstructed actuator dynamics.

The experimental setup for the fixed-free boundary condition is shown in Fig. 4. The fixed-free boundary condition was obtained by gluing the bottom of the actuator to a stable vibro-isolated mass. The mass was sufficient ($>10\text{kg}$) to be regarded as a stationary/fixed support. The acceleration of the free end was measured with an accelerometer that was glued to the PLA spacer on the top of the actuator. PLA spacer was printed with the actuator. It distanced the sensor from the top electrode to reduce the electromagnetic noise picked up from the electrically excited actuator and provided a stiff and flat surface for the sensor [27]. In this case the load was the mass of the accelerometer (5 g) with a negligible effect on the response (the inertial load was significantly smaller than the generated force).

A PCB 356A32 3-axis IEPE piezoelectric accelerometer (PCB Piezotronics, USA) was used for an uncoupled measurement of the vertical (longitudinal contraction) and horizontal (bending) actuator dynamics. The sensor signal was acquired with a National Instruments measuring chain comprised of an NI9234 DAQ card and an NI cDAQ-9174 chassis.

The measured time signals were transformed into the frequency domain by the Fourier transform (FT). The actuator's dynamic characteristic was calculated as a ratio of the FT of the response to the FT of the squared excitation voltage. This enabled a linear representation of the dynamic characteristic of a quadratic, nonlinear, electromechanical coupling.

The fixed-free electromechanical characteristic was defined as the acceleration A divided by the FT of the squared excitation voltage V_{sq} :

$$H_{\text{a,v}}(\omega) = \frac{A(\omega)}{V_{\text{sq}}(\omega)} \left[\frac{\text{m/s}^2}{\text{V}^2} \right], \quad (8)$$

and as displacement X divided by the FT of the squared excitation voltage V_{sq} :

$$H_{\text{x,v}}(\omega) = \frac{X(\omega)}{V_{\text{sq}}(\omega)} \left[\frac{\text{m}}{\text{V}^2} \right], \quad (9)$$

where ω is the angular velocity. The displacement X was calculated in the frequency domain from the measured acceleration A :

$$X(\omega) = -\frac{A(\omega)}{\omega^2}. \quad (10)$$

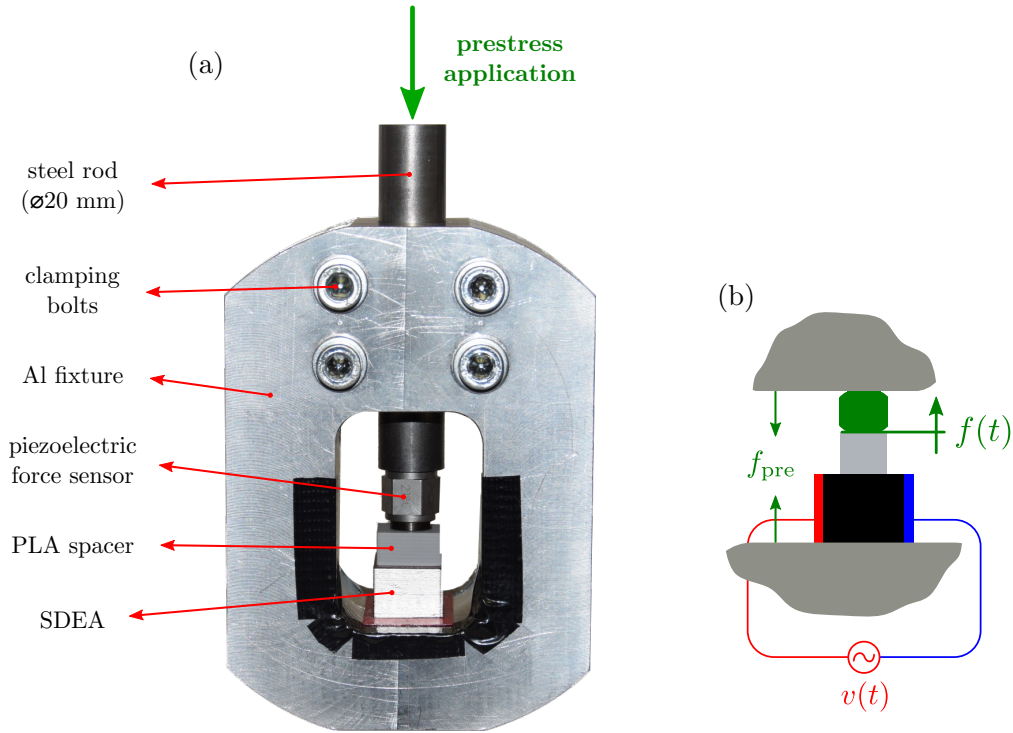


Figure 5: **Experimental setup for dynamic blocked-force characterization.** (a) An actuator is placed into the fixture and a pre-stress force is applied by the steel rod with a piezoelectric force sensor on the tip. The rod is clamped with the clamping bolts into the fixture. (b) Front view sketch of the characterization setup with the electrical connection $v(t)$, pre-stress force f_{pre} , and generated force $f(t)$.

5.2. Blocked-force characterization

The fixed-fixed or blocked-force characterization makes it possible to analyse the generated force in a simulated, infinite-load condition. Because the strain of the actuator is blocked, the measured force should not exhibit any actuator dynamics. The fixed-fixed boundary condition was achieved with an aluminium fixture, shown in Fig. 5. The actuator was placed inside the fixture and the force sensor, mounted to the steel rod, was lowered onto the PLA spacer.

When the actuator is active it is contracted; therefore, a static pre-stress is required to measure the generated force. The static pre-stress was applied via the steel rod (Fig. 5) and the static force was measured. When the desired pre-stress force was achieved, the steel rod was fixed in the tight-fit with the

clamping bolts. The whole setup shown in Fig. 5 was then placed onto a vibro-isolated surface and dynamically characterized. To reduce the effect of the viscoelastic relaxation (reduction of the pre-stress) in the actuator, the characterization was made immediately after pre-stressing.

The magnitude of the pre-stress force was determined with an electromechanical characterization of an actuator, while incrementally increasing the pre-stress force by 200 N, starting at 100 N. For each step, the time-domain and frequency-domain responses were examined. In the case of a small pre-stress, the response was non-linear due to the separation between the contact surfaces between the actuator and the fixture. In contrast, a high pre-stress reduces the dielectric strength of the actuator by compressing the dielectric layers and increasing the electric field. This in turn increases the pull-in electromechanical instability [50] that can result in a dielectric breakdown of the actuator. For the actuators in this study, the linear response was achieved at pre-stress force of 1 kN.

The static pre-stress force and the dynamic actuator force were measured with a PCB 218C piezoelectric force sensor. The static charge (from the static pre-stress force) was amplified with a Kistler 5073A charge amplifier (Kistler Group, Switzerland). The dynamic charge (actuator response) was amplified with a Nexus 2692 charge amplifier (Brüel & Kjær, Denmark). The generated voltage from the charge amplifiers were measured with an NI9232 DAQ card.

The frequency range of the blocked-force characterization needs to be well below the resonance of the experimental system. The first natural frequency of the system was identified from the frequency-response functions. The setup was excited with an impact hammer, coaxially with the steel rod. The response was measured with an accelerometer fixed to the experimental fixture in parallel with the excitation direction. The first resonance of the setup with and without the pre-stressed sample was measured to be around 5 kHz. Therefore, the characterization range from 100 Hz to 2 kHz was not affected by the dynamics of the fixture.

To research the inertial influences, the acceleration of the sensor's base plate was measured with an impedance probe (PCB 288D01). The measured acceleration of the sensor's base plate was below 0.03 m/s^2 in the complete characterization frequency range. As the dynamically attached mass of the impedance probe is 4.8 g, the inertial force can be estimated to be below 0.14 mN (significantly below the later measured dynamic force).

The fixed-fixed electromechanical characteristic was defined as the dy-

dynamic force F divided by the FT of the squared excitation voltage V_{sq} :

$$H_{f,v}(\omega) = \frac{F(\omega)}{V_{\text{sq}}(\omega)} \left[\frac{\text{N}}{\text{V}^2} \right]. \quad (11)$$

6. Results

Firstly, the results of the electrical characterization are presented, including the measured electrical impedance and capacitance of each actuator. Secondly, the electromechanical characteristics of each actuator are presented and discussed, including the comparison of the actuator’s performance. The free-displacement (fixed-free) and blocked-force (fixed-fixed) characteristics are presented sequentially in the time and frequency domains.

Samples included in the results are defined in Tab. 1, including the theoretical capacitance explained in Sec. 6.1

Table 1: Samples with corresponding dimensions and theoretical capacitance $C_{\text{theor.}}$.

sample	DE layer thickness [mm]	num. of DE layers	active area [mm×mm]	active area [mm ²]	$C_{\text{theor.}}$ [nF]
N50-A15x15	0.15	50	15×15	225	3.59
N50-A20x20	0.15	50	20×20	440	6.37
N100-A15x15	0.15	100	15×15	225	7.17
N100-A20x20	0.15	100	20×20	440	12.75

6.1. Electrical characteristic

The measured electrical impedance and capacitance of each sample actuator are shown in Fig. 6. The characterization was performed from 100 Hz to 20 kHz.

The plotted impedance in polar form (magnitude in Fig. 6a and phase in Fig. 6b) exhibits close-to-pure capacitance properties. The resistivity of the NT Eel filament was measured at $0.13 \Omega\text{m}$ (7 orders of magnitude greater than copper). Despite the large resistance of the electrode material, the charging of the dielectric layers was not limited in the characterised frequency range (i.e. cutoff frequency is higher than 20 kHz).

The capacitance of the actuators (see Fig. 6c) is influenced by the active area A , the dielectric layer thickness d , the dielectric permittivity ϵ ,

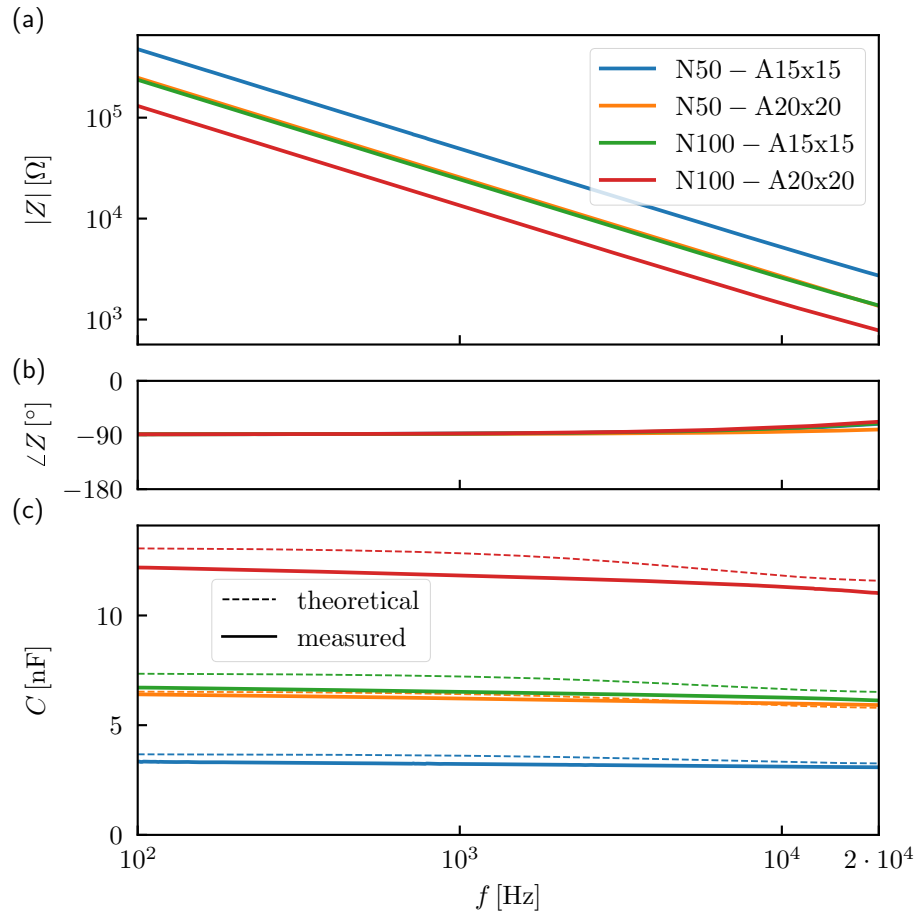


Figure 6: **Results of electrical characterization:** (a) the magnitude of the electrical impedance Z of all samples (logarithmic scale, shared x-axis), (b) the phase of the electrical impedance, (c) the measured capacitance of each sample and the theoretical capacitance calculated from the dimensions of the actuators and the measured relative permittivity of the dielectric.

and the number of active layers N . All samples (Tab. 1) were printed with the same material, conditions and dielectric thickness. Therefore, A and N are the variables that determine the actuators' capacitance. As expected, the N100-A20x20 actuator exhibits the highest capacitance (12.2 nF), N50-A20x20 and N100-A15x15 exhibit comparable capacitances (6.4 and 6.7 nF, respectively), and the smallest actuator N50-A15x15 exhibits the lowest capacitance (3.3 nF). Although N50-A20x20 and N100-A15x15 are comparable in electrical characteristics, the electromechanical response differs, as will be shown in Sec. 6.2.

The gradual decrease in capacitance with frequency is the result of frequency-dependent polarization mechanisms in the dielectric and is typical for the materials used in dielectric actuation.

The permittivity of the TPU was determined in the preliminary experiments where the capacitance of one active unit (one DE layer) was measured (for Trcek TPU $\epsilon_r = 5.4$). The known permittivity of the dielectric was used to estimate the theoretical capacitance of each actuator based on the specified dimensions (see Tab. 2 and Fig. 6c - dashed lines). Comparing the expected and measured capacitance gives an indirect measure of the fabrication accuracy and reliability. The capacitance lower than expected can be attributed to the thicker dielectric layers and the electrodes with compromised electrical contacts (dielectric regions without charge).

6.2. Electromechanical characteristic

The response amplitudes are presented in Tab. 2, to provide a practical

Table 2: Response amplitudes of each sample driven at 60 V.

sample	f_{res} [kHz]	$ a $ (at f_{res}) [m/s ²]	$ x $ (at 500 Hz) [nm]	$ x $ (at f_{res}) [nm]	$ f $ (at 200 Hz) [mN]
N50-A15x15	2.75	0.82	1.74	2.92	5.7
N50-A20x20	2.80	1.19	2.08	3.97	7.8
N100-A15x15	2.00	0.90	3.04	6.29	5.4
N100-A20x20	2.05	1.16	3.39	7.55	8.3

representation of the performance of each actuator. The dynamic response of an actuator in a fixed-free boundary condition exhibits a resonance frequency f_{res} where the response reaches a peak amplitude (see Sec. 6.2.1). Fixed-free acceleration a and displacement x for the sub-resonance (500 Hz) and

resonance frequencies f_{res} and the force f at 200 Hz are provided (Tab. 2). To enable a direct comparison between the samples, all samples were driven with an AC voltage with a constant amplitude of 60 V.

The results presented in Tab. 2 are explained with the corresponding actuator characteristics in Figs. 7, 8, 9, and 10.

6.2.1. Fixed-free response

Fig. 7 provides the characterization results for the N100-A20x20 actuator showing the time signals and transformation into the frequency domain with the corresponding frequency characteristics of all the measured variables. The driving voltage v (Fig. 7a), squared driving voltage v^2 (Fig. 7b), and the response of the actuator as acceleration a (Fig. 7c) are provided in the time domain on the left-hand side and the frequency domain on the right-hand side of Fig. 7. The time-domain signals are plotted for the sub-resonance (0.5 kHz), in-resonance (1 kHz), and sup-resonance (1.5 kHz) excitation frequencies. The frequency domain plots of the driving voltage V , squared driving voltage V_{sq} , and acceleration A magnitude are plotted in the complete characterization frequency range. The squared driving voltage in the time and frequency domains is added as a visual aid for the representation of the quadratic electromechanical coupling (Maxwell pressure) and the doubled excitation frequency in the response.

The time-domain signals show that the AC driving voltage produces a clear sine-wave response, exhibiting the desired dynamic applicability of the 3D-printed actuator. The time delay between the driving voltage and response can be distinguished from the time-domain signals, but will be better represented in the frequency domain, see Fig. 8.

Fig. 8 presents electromechanical frequency characteristics (response normalised by excitation), which enable a direct comparison of the dynamic properties and performance of each actuator. The FT of the driving voltage clearly shows a constant driving amplitude in the complete frequency range. As expected, the acceleration (and displacement) shows a frequency dependent response.

Fig. 8a shows the acceleration characteristic $H_{a,v}$ and Fig. 8b shows the displacement characteristic $H_{x,v}$, both consisting of magnitude and phase components. Depending on the desired application of the actuator a knowledge of $H_{a,v}$ or $H_{x,v}$ are needed, e.g., $H_{a,v}$ is required to investigate the active vibroisolation functionality, $H_{x,v}$ is needed for dynamic nanopositioning functionality.

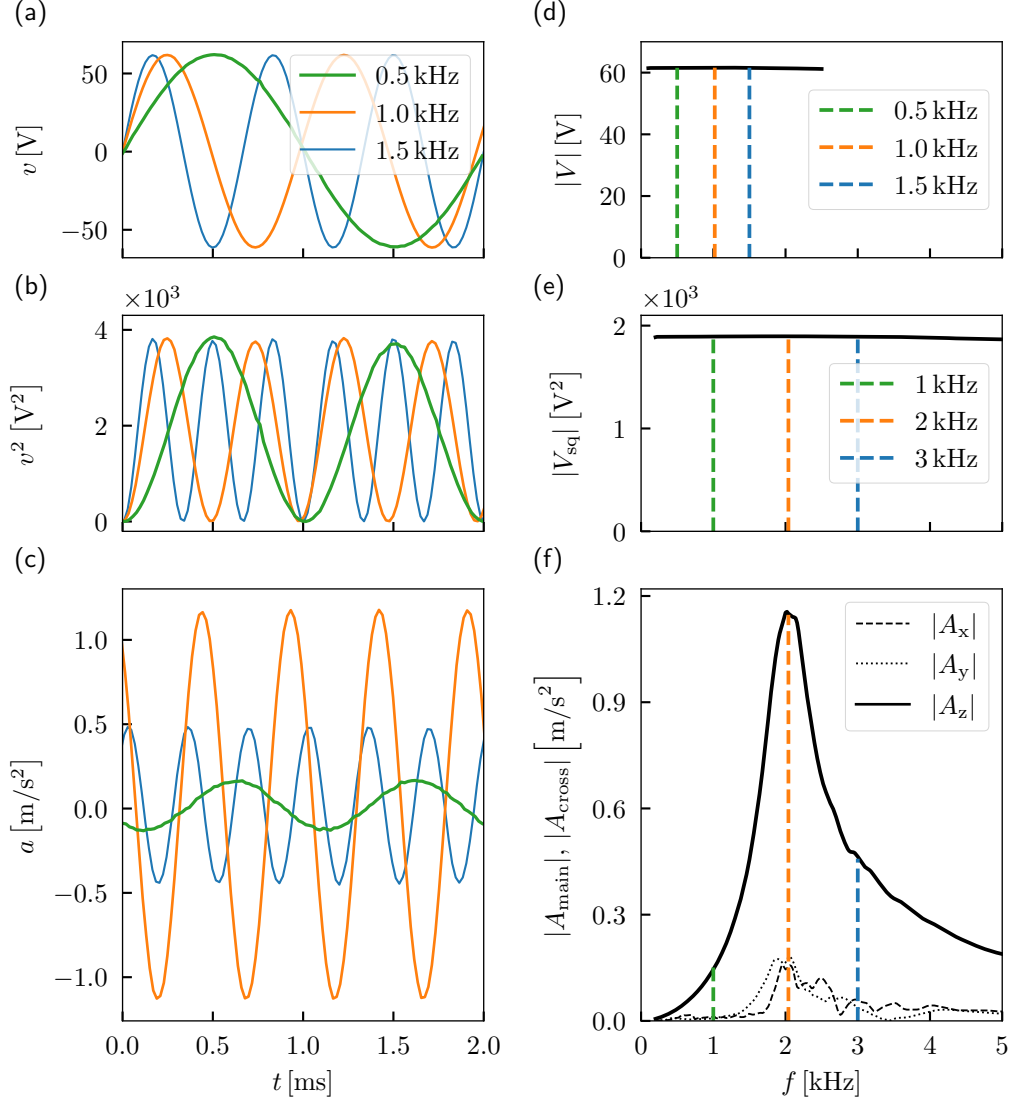


Figure 7: **N100-A20x20 sample in a fixed-free boundary condition:** (a) driving voltage in the time domain for three discrete excitation frequencies (0.5 kHz, 1 kHz, 1.5 kHz), (b) squared driving voltage for graphical representation of the quadratic electro-mechanical coupling, (c) measured acceleration in the time domain, (d) frequency characteristic of the driving voltage for the complete frequency excitation set (100 Hz to 2.5 kHz) (e) frequency characteristic of the squared driving voltage (the frequency is doubled), (f) frequency characteristic of the acceleration for the primary compression response (A_z) and the bending responses (A_x and A_y).

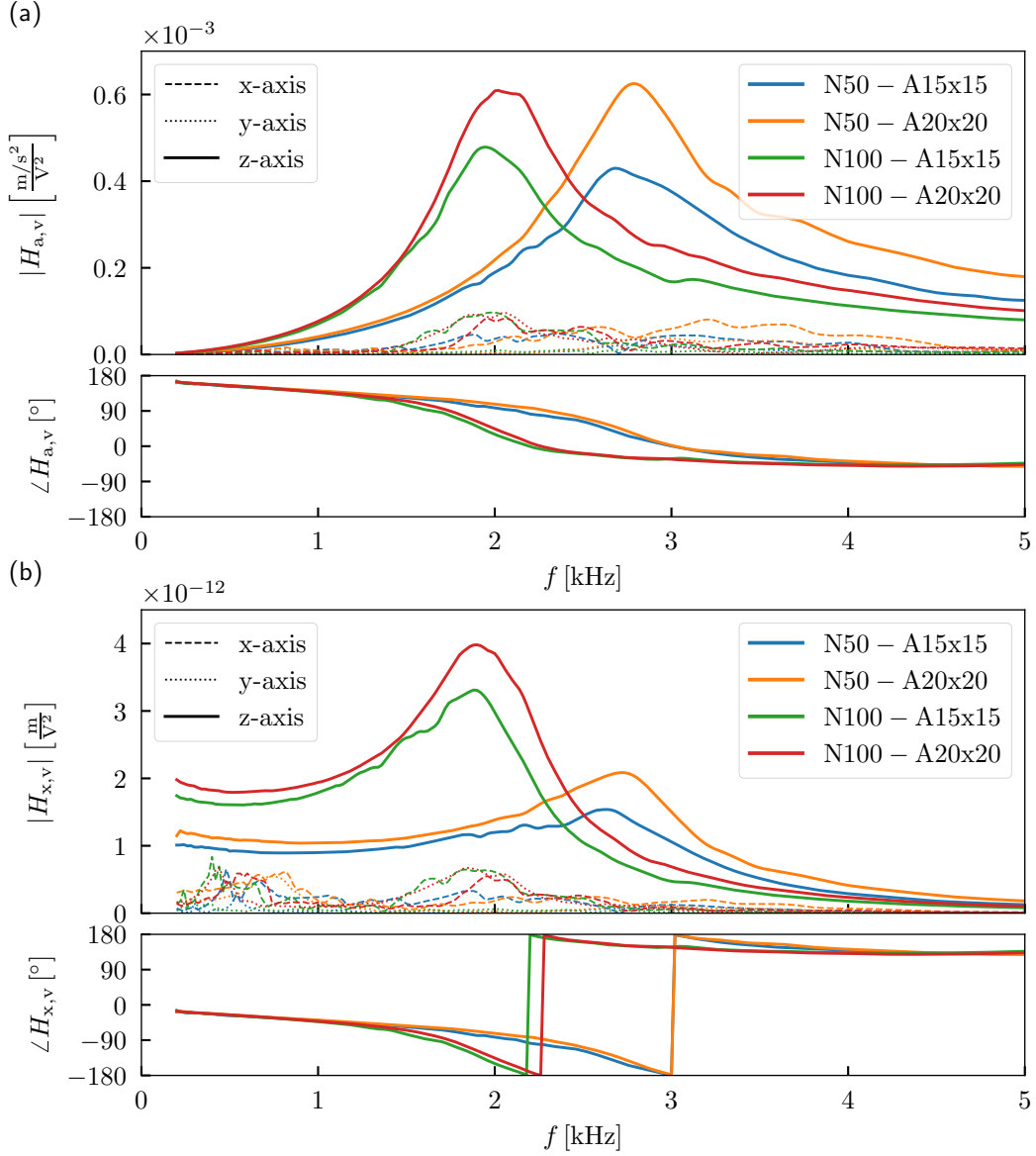


Figure 8: **Free-displacement electromechanical frequency characteristics.** (a) The magnitude $|H_{a,v}|$ and phase $\angle H_{a,v}$ of the acceleration frequency characteristics of each actuator for the compression (z-axis) and bending (x-axis and y-axis) responses. (b) The magnitude $|H_{x,v}|$ and phase $\angle H_{x,v}$ of the displacement frequency characteristics of each actuator for the compression (z-axis) and bending (x-axis and y-axis) responses.

All samples exhibit a typical dynamic characteristic of an actuator with a pronounced first harmonic (at ~ 2 and 3 kHz). Higher harmonics are not evident in the characterization frequency range. The resonance frequency is dependent on the structural dynamics of the actuator. Here, it is directly proportional to the active area A and inversely proportional to the height (the number of active layers N) of the actuator. The $H_{a,v}$ magnitude at the resonance frequency is mainly dependent on the active area A .

$H_{x,v}$ shows a close-to-constant magnitude in the sub-resonance region. The resonance produces roughly twice the displacement amplitude compared to the sub-resonance region. Actuators with 100 layers respond with twice the amplitude of the 50-layer actuators in the sub-resonance region.

The plotted phases of $H_{a,v}$ and $H_{x,v}$ show a constant increase in the response delay, which can be expected for thermoplastic elastomers exhibiting frequency-dependent stiffness and high internal damping [72].

The cross-axis x- and y-axis acceleration amplitudes (bending) are the highest at the resonance frequency, reaching $\sim 15\%$ of the z-axis acceleration (the primary actuation direction). The cross-axis excitation of the actuator is the result of multiple factors, for example, the variation of the material stiffness and the density as a result of the extrusion/deposition process, the variation in the Maxwell pressure as a result of different dielectric thicknesses, and deviation of the sensor positioning with respect to the symmetry line.

6.2.2. Fixed-fixed response

Fig. 9 shows the time and the frequency domain of the measured excitation and response signals for the N100-A20x20 actuator in a fixed-fixed boundary condition.

The actuator exhibits a clear harmonic response (Fig. 9c) confirming the high frequency dynamic applicability of the 3D-printed actuators. The magnitude of the excitation (V and V_{sq}) is constant. The magnitude of the actuating force F exhibits a gradual decrease. Although, the force magnitude is not constant, no resonance can be observed. This confirms the effective blocking of the actuator dynamics with the proposed characterization method.

Fig. 10 shows the blocked-force frequency characteristic $H_{f,v}$ of each printed actuator. It is evident that the actuating force in a blocked configuration is primarily dependent on the active area A . Actuators with equal active areas have more similar characteristics. Actuators with a 400 mm^2 active area (+44% compared to 225 mm^2) exhibit $\sim 30\%$ increase in the generated force.

The applied pre-stress of 1 kN and the constrained boundary surfaces

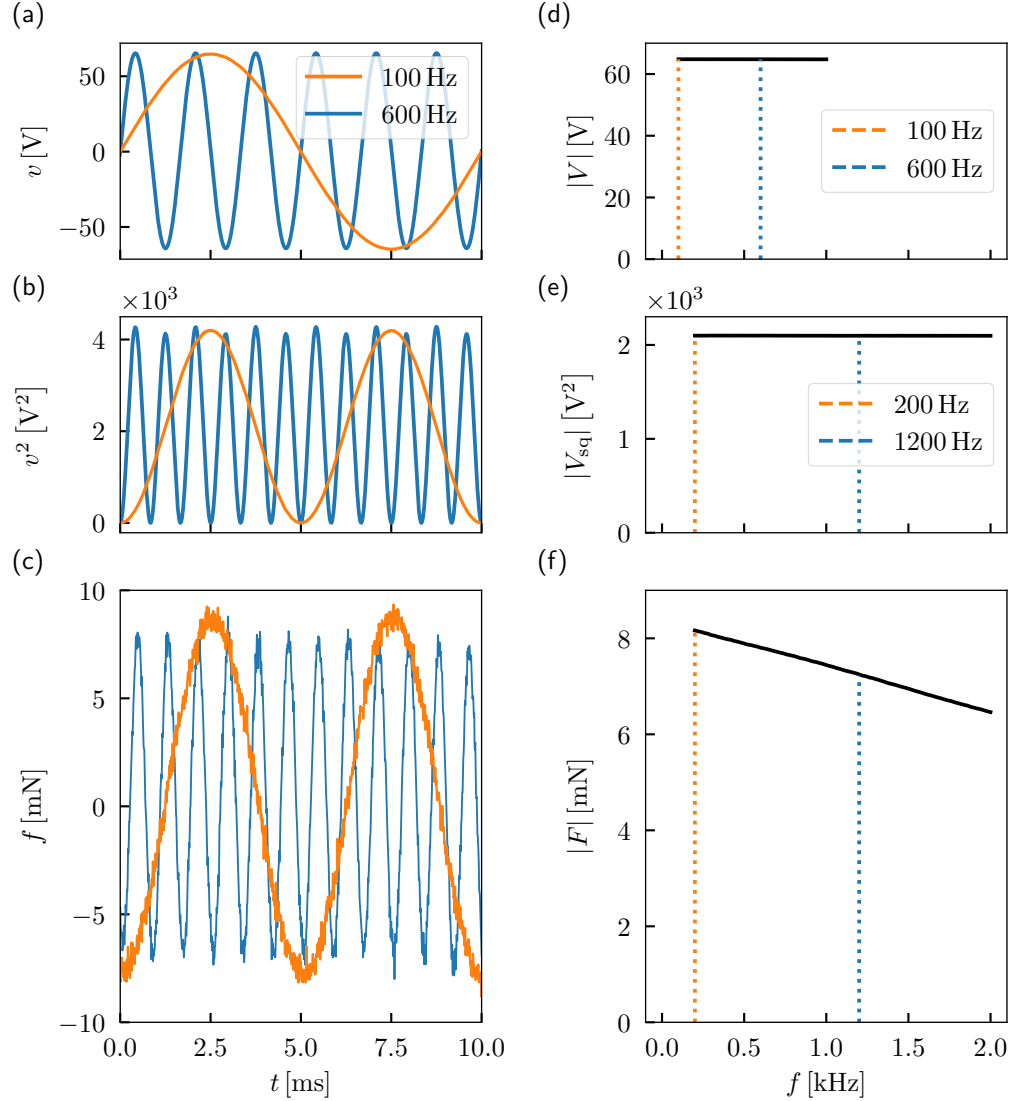


Figure 9: **N100-A20x20 sample in a fixed-fixed boundary condition:** (a) driving voltage in the time domain for two discrete excitation frequencies (100 Hz, 600 Hz), (b) squared driving voltage for a graphical representation of the quadratic electro-mechanical coupling, (c) measured force in the time domain for the two excitation frequencies, (d) frequency characteristic of the driving voltage for the complete frequency-excitation set (100 Hz to 1 kHz), (e) frequency characteristic of the squared driving voltage (the frequency is doubled), (f) frequency characteristic of the force response.

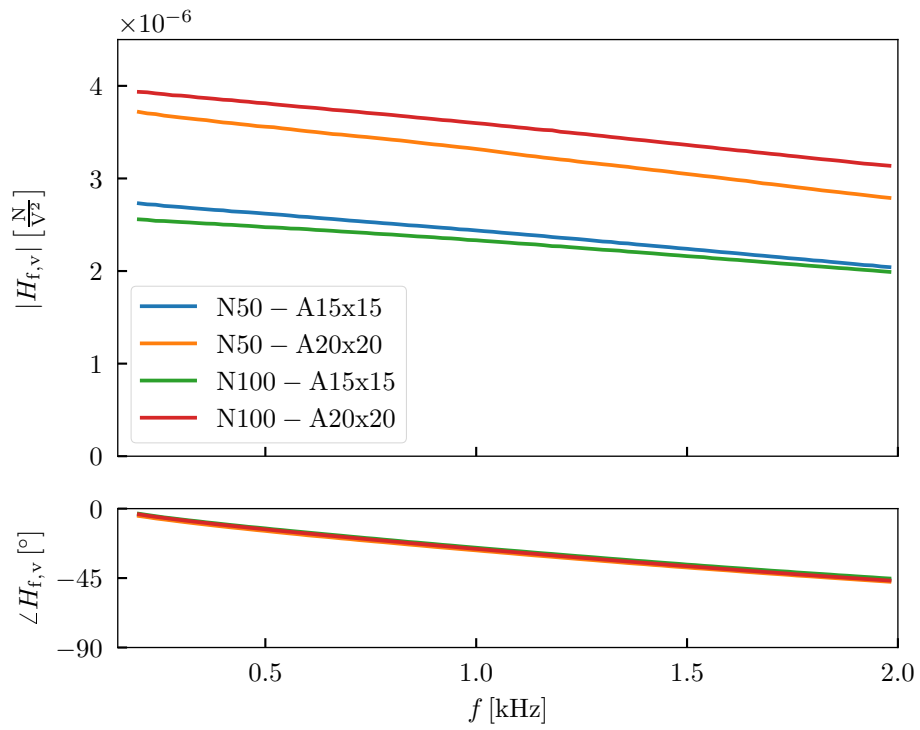


Figure 10: **Blocked-force electromechanical frequency characteristics** in magnitude $|H_{f,v}|$ and phase $\angle H_{f,v}$ form for each actuator.

increase the resonance frequencies of an actuator. Nevertheless, the magnitude and phase of the responses are not exactly constant. The gradually decreasing actuating force in the frequency domain can be attributed to electrical and dynamical factors. The frequency-dependent relative permittivity $\epsilon_r(\omega)$ of the dielectric will affect the generated force (see Eq. (3)). The dynamic effect can be attributed to the strains in the non-constrained layers of the actuator. Although the strains are small, the effects of the dynamic properties of the thermoplastic elastomers (TPEs) can be observed in the measurements.

The gradual decrease in the generated force can be attributed to a decreasing permittivity and capacitance of the actuator (see Fig. 6c). Additionally, the elastic modulus of the TPU material can decrease the measured force with an increasing excitation frequency. Elastomers exhibit a frequency-dependent elastic modulus, which increases with the strain frequency [72]. With increasing frequency, the material becomes stiffer and the consequent strain of the actuator is reduced. As a result, the generated dynamic force is reduced with the frequency.

In the fixed-free and fixed-fixed boundary conditions, a constant delay in the response is evident, which is due to the internal damping of the TPEs.

7. Discussion

The results clearly show the typical electromechanical behaviour of a stacked dielectric actuator. The electrical characteristics exhibit RC circuit properties with a relatively high capacitance. The dynamic response includes pronounced resonance regions with high damping.

The permittivity of the utilised TPU material is comparable to the classical elastomers for dielectric actuation (silicones $\epsilon_r \approx 3$, polyurethanes $\epsilon_r \approx 7$, 3M VHB 4910 $\epsilon_r = 4.8$) [73]. The used conductive TPU composite demonstrated sufficient conductivity for a relatively high-frequency dynamic operation (the charging of the dielectric layer was not significantly restricted up to 20 kHz). However, the low conductivity of the electrodes could result in a heating problem when the actuator would be subjected to long-term and high-demand operation.

The proposed characterization methods for fixed-free and fixed-fixed boundary conditions provided a comprehensive insight into the dynamic performance of the 3D-printed actuators.

The results of the free displacement characterization show an applicable dynamic operation in the sub-resonance and resonance regions. The sub-resonance frequency region exhibits a relatively close-to-constant characteristic enabling great controllability and repeatability of the dynamic operation. This can be utilised in vibro-isolating and vibro-acoustic applications, for which DEAs have already proven to be uniquely practical [74]. The resonance response can be utilised for applications that require a narrow operational frequency region. In this region, higher strains and forces can be achieved, increasing the actuator’s efficiency. Furthermore, the individualisation advantage of 3D-printed structures can provide actuators with a precisely tailored dynamic response. Furthermore, 3D printing makes it possible to fabricate secondary structures with the actuator. These additional structures (e.g., bridge amplification and bistable compliant mechanisms) can modify and amplify the response of the actuator, adapting it for a specific requirement and increasing its efficiency.

It is important to consider that the electromechanical characteristic of a SDEA is strongly dependent on the load itself. For that reason, it is best to adapt the actuator to a specific application and associated load conditions. The blocked-force characterization presented in this manuscript has shown that a printed SDEA is capable of dynamic operation over a broad frequency range with a conveniently (close-to-)constant frequency characteristic. This means the actuator can be useful for demanding applications requiring high controllability and a fast response. However, the importance of understanding the materials’ frequency- and amplitude-dependent viscoelastic properties must not be overlooked. Further research of the material properties and the effects of different load conditions needs to be performed to enable an implementation of the 3D-printed SDEAs.

The comparison of the presented and existing stacked dielectric actuators in the research literature is difficult because of multiple factors that vary between the scientific papers. Firstly, the variation in materials and material combinations with different electrical (permittivity) and mechanical properties (stiffness, damping) has a profound effect on the electromechanical characteristic of the actuator. Secondly, the actuator dimensions, the number of layers, and the layer thicknesses also affect the resulting performance. Lastly, the characterization method including the operation regime (static/dynamic), actuator mounting (pre-strain [75], loading), electrical excitation, and the representation of actuator’s characteristic are specific for each contribution.

The main limiting factors of the presented actuators are relatively low flexibility of the printable TPU materials and the thickness of the dielectric layers. With this in mind, the presented 3D-printed actuators exhibit electromechanical displacement and force characteristics comparable to recent SDEA contributions fabricated with manual [46] and automatic techniques [76].

The constant development of printable polymer composites with functional electrical, dielectric, and mechanical properties indicates that the performance of 3D-printed active structures will only improve. For performance advancement in active dielectric structures, the flexibility of 3D-printed structures is increasing with technological and material advances [77]. The permittivity of dielectrics is increasing with recently developed polymer composites that have chemical modifications and ferroelectric fillers [78, 79]. The conductivity of polymer nanocomposites is steadily improving with a better understanding of percolation mechanisms and the nano-assembly of the conductive networks in the polymer matrix [54]. Furthermore, multiple 3D-printing technologies can be combined into a single machine to broaden the material assortment [69]. For instance, DIW can be simply combined with FFF technology in a single machine to provide the deposition of softer polymers and polymer composites for the electrodes or dielectric layers [80]. Furthermore, recent research into field-assisted additive manufacturing can provide improvements in the functional (e.g., electroactive, conductive) and mechanical properties [81].

Existing electromechanical analytical and numerical models can provide a foundation for the prediction of the 3D-printed actuator's characteristics and enable simulation in various boundary and load conditions. The flexibility of the presented manufacturing strategy can be utilised for time-efficient model validation with various actuator specifications (dimensions and printing parameters), load conditions, and driving-voltage signals.

8. Conclusions

It can be concluded that FFF 3D-printing technology with commercial materials provides an attractive fabrication method with unmatched advantages over the classical approached, for example, individualization of the shape, dimensions, and electromechanical characteristics, printing of multiple actuators with various dimensions and materials in a single process, and

embedding of an actuator into a 3D-printed structure with passive and active components printed in parallel (e.g. 3D-printed sensors [26]).

The main challenge is in the reliability, accuracy, and repeatability of the thermoplastic elastomer's extrusion and deposition. This research showed that typical 3D-printing issues (e.g., inconsistent thickness, uneven surface, and porosity) can be mitigated.

With rigorous control of the printing process and the advancement of inspection systems the accuracy and repeatability can be further increased. Inspection systems generating feedback for the extrusion and deposition process provide live, quantitative indicators of the quality of the deposited layers, further increasing the capabilities of the FFF technology in the field of active multifunctional structures.

The presented electromechanical characterization methods for dynamic operation in a free and fixed condition are effective in a broad frequency range (up to 5 kHz) and provide a foundation for the analysis of SDEAs for vibro-acoustic and dynamic nano-positioning applications.

The presented actuators have been shown to exhibit functional dynamic operation. Free and fixed frequency characteristics show broad, near-constant operational regions. 3D-printed SDEAs, therefore, show a promising applicability in vibro-acoustic applications where controllable and repeatable dynamic operation is required. To achieve higher response amplitudes and efficiency, the narrow resonance region can be excited, showing promise in specific applications that require a narrow operating range for the frequency.

The first dynamic DEAs 3D printed with accessible FFF technology and materials in a single process reveal new possibilities in the field of individualised, multi-functional active structures.

Acknowledgements

The authors acknowledge the partial financial support from the Slovenian Research Agency (research core funding No. P2-0263 and research project J2-3045).

References

- [1] D. Ni, R. Heisser, B. Davaji, L. Ivy, R. Shepherd, A. Lal, Polymer interdigitated pillar electrostatic (PIPE) actuators, *Microsystems & Nanoengineering* 8 (1) (2022) 18. doi:10.1038/s41378-021-00328-0.

- [2] M. Osada, G. Zhang, F. Carneiro, M. Muromachi, S. Yoshimoto, A. Yamamoto, Effect of insulating liquid viscosity on output force of a high-power synchronous electrostatic motor, *International Journal of Mechanical Sciences* 220 (2022) 107149. doi:10.1016/j.ijmecsci.2022.107149.
- [3] Y. Huang, J. Chen, M. Zhao, M. Feng, Electromechanical coupling characteristics of double-layer piezoelectric quasicrystal actuators, *International Journal of Mechanical Sciences* 196 (2021) 106293. doi:10.1016/j.ijmecsci.2021.106293.
- [4] R. S. Reddy, S. Panda, A. Gupta, Nonlinear dynamics and active control of smart beams using shear/extensional mode piezoelectric actuators, *International Journal of Mechanical Sciences* 204 (2021) 106495. doi:10.1016/j.ijmecsci.2021.106495.
- [5] X. Cao, S. Xuan, Y. Gao, C. Lou, H. Deng, X. Gong, 3D Printing Ultraflexible Magnetic Actuators via Screw Extrusion Method, *Advanced Science* 9 (16) (2022) 2200898. doi:10.1002/adv.202200898.
- [6] A. D. Charles, A. N. Rider, S. A. Brown, C. H. Wang, Multifunctional magneto-polymer matrix composites for electromagnetic interference suppression, sensors and actuators, *Progress in Materials Science* 115 (2021) 100705. doi:10.1016/j.pmatsci.2020.100705.
- [7] H. Tiismus, A. Kallaste, T. Vaimann, A. Rassõlkin, State of the art of additively manufactured electromagnetic materials for topology optimized electrical machines, *Additive Manufacturing* 55 (2022) 102778. doi:10.1016/j.addma.2022.102778.
- [8] Y. Jang, H. Nabae, G. Endo, K. Suzumori, Analysis of the multi-balloon dielectric elastomer actuator for traveling wave motion, *Sensors and Actuators A: Physical* 333 (2022) 113243. doi:10.1016/j.sna.2021.113243.
- [9] P. Kumar, B. Muralidharan, D. N. Pawaskar, M. M. Inamdar, Investigation of phonon lasing like auto-parametric instability between 1-D flexural modes of electrostatically actuated microbeams, *International Journal of Mechanical Sciences* 220 (2022) 107135. doi:10.1016/j.ijmecsci.2022.107135.

- [10] T. Hiruta, N. Hosoya, S. Maeda, I. Kajiwara, Experimental validation of vibration control in membrane structures using dielectric elastomer actuators in a vacuum environment, *International Journal of Mechanical Sciences* 191 (2021) 106049. doi:10.1016/j.ijmecsci.2020.106049.
- [11] E. Garnell, C. Rouby, O. Doaré, Dynamics and sound radiation of a dielectric elastomer membrane, *Journal of Sound and Vibration* 459 (2019) 114836. doi:10.1016/J.JSV.2019.07.002.
- [12] L. Medina, A. A. Seshia, Tristable properties and limit point behaviour in electrostatically actuated initially curved coupled micro beams, *International Journal of Mechanical Sciences* 204 (2021) 106543. doi:10.1016/j.ijmecsci.2021.106543.
- [13] B. Sparrman, C. du Pasquier, C. Thomsen, S. Darbari, R. Rustom, J. Laucks, K. Shea, S. Tibbits, Printed silicone pneumatic actuators for soft robotics, *Additive Manufacturing* 40 (2021) 101860. doi:10.1016/J.ADDMA.2021.101860.
- [14] T. Hanuhov, N. Cohen, Thermally induced deformations in multi-layered polymeric struts, *International Journal of Mechanical Sciences* 215 (2022) 106959. doi:10.1016/j.ijmecsci.2021.106959.
- [15] O. Ulkir, Design and fabrication of an electrothermal MEMS micro-actuator with 3D printing technology, *Materials Research Express* 7 (7) (2020) 075015. doi:10.1088/2053-1591/aba8e3.
- [16] F. Long, Y. Cheng, Y. Ren, J. Wang, Z. Li, A. Sun, G. Xu, Latest Advances in Development of Smart Phase Change Material for Soft Actuators, *Advanced Engineering Materials* 24 (3) (2022) 2100863. doi:10.1002/adem.202100863.
- [17] Z. Zhao, K. Wang, L. Zhang, L.-C. Wang, W.-L. Song, D. Fang, Stiff reconfigurable polygons for smart connectors and deployable structures, *International Journal of Mechanical Sciences* 161-162 (2019) 105052. doi:10.1016/j.ijmecsci.2019.105052.
- [18] A. M. Soomro, F. H. Memon, J.-W. Lee, F. Ahmed, K. H. Kim, Y. S. Kim, K. H. Choi, Fully 3D printed multi-material soft bio-inspired frog

- for underwater synchronous swimming, *International Journal of Mechanical Sciences* 210 (2021) 106725. doi:10.1016/j.ijmecsci.2021.106725.
- [19] G. Zhong, W. Dou, X. Zhang, H. Yi, Bending analysis and contact force modeling of soft pneumatic actuators with pleated structures, *International Journal of Mechanical Sciences* 193 (2021) 106150. doi:10.1016/j.ijmecsci.2020.106150.
- [20] W. Xiao, X. Du, W. Chen, G. Yang, D. Hu, X. Han, Cooperative collapse of helical structure enables the actuation of twisting pneumatic artificial muscle, *International Journal of Mechanical Sciences* 201 (2021) 106483. doi:10.1016/j.ijmecsci.2021.106483.
- [21] L. M. Fonseca, G. V. Rodrigues, M. A. Savi, An overview of the mechanical description of origami-inspired systems and structures, *International Journal of Mechanical Sciences* 223 (2022) 107316. doi:10.1016/j.ijmecsci.2022.107316.
- [22] A. Georgopoulou, L. Egloff, B. Vanderborght, F. Clemens, A Soft Pneumatic Actuator with Integrated Deformation Sensing Elements Produced Exclusively with Extrusion Based Additive Manufacturing, in: *The 8th International Symposium on Sensor Science*, MDPI, 2021, p. 11. doi:10.3390/I3S2021Dresden-10097.
- [23] T. Hainsworth, L. Smith, S. Alexander, R. MacCurdy, A Fabrication Free, 3D Printed, Multi-Material, Self-Sensing Soft Actuator, *IEEE Robotics and Automation Letters* 5 (3) (2020) 4118–4125. doi:10.1109/LRA.2020.2986760.
- [24] M. Arh, J. Slavič, Single-Process 3D-Printed Triaxial Accelerometer, *Advanced Materials Technologies* (2021) 2101321doi:10.1002/admt.202101321.
- [25] T. Košir, J. Slavič, Single-process fused filament fabrication 3D-printed high-sensitivity dynamic piezoelectric sensor, *Additive Manufacturing* 49 (2022) 102482. doi:10.1016/j.addma.2021.102482.
- [26] H. Watschke, M. Goutier, J. Heubach, T. Vietor, K. Leichsenring, M. Böhl, Novel Resistive Sensor Design Utilizing the Geometric Free-

- dom of Additive Manufacturing, *Applied Sciences* 11 (1) (2020) 113. doi:10.3390/app11010113.
- [27] M. Palmieri, G. Zucca, G. Morettini, L. Landi, F. Cianetti, Vibration Fatigue of FDM 3D Printed Structures: The Use of Frequency Domain Approach, *Materials* 15 (3) (2022) 854. doi:10.3390/MA15030854.
- [28] X. Wei, H. Li, X. He, Z. Li, H. Ye, W. Xue, Q. Ge, Shape Memory Polymer-based Stiffness Variable Soft Actuator Via Digital Light Processing-based 3D Printing, in: 2021 27th International Conference on Mechatronics and Machine Vision in Practice (M2VIP), 2021, pp. 612–616. doi:10.1109/M2VIP49856.2021.9665032.
- [29] L. Fang, T. Röddiger, H. Sun, N. Willenbacher, M. Beigl, FLECTILEE: 3D-Printable Soft Actuators for Wearable Computing, in: Proceedings of the 2020 International Symposium on Wearable Computers, ACM, 2020, pp. 32–36. doi:10.1145/3410531.3414307.
- [30] T. B. Palmić, J. Slavič, M. Boltežar, Process parameters for fff 3d-printed conductors for applications in sensors, *Sensors (Switzerland)* 20 (16) (2020) 1–21. doi:10.3390/s20164542.
- [31] Z. Lei, Z. Chen, Y. Zhou, Y. Liu, J. Xu, D. Wang, Y. Shen, W. Feng, Z. Zhang, H. Chen, Novel electrically conductive composite filaments based on Ag/saturated polyester/polyvinyl butyral for 3D-printing circuits, *Composites Science and Technology* 180 (2019) 44–50. doi:10.1016/J.COMPSCITECH.2019.05.003.
- [32] C. Reyes, R. Somogyi, S. Niu, M. A. Cruz, F. Yang, M. J. Catenacci, C. P. Rhodes, B. J. Wiley, Three-Dimensional Printing of a Complete Lithium Ion Battery with Fused Filament Fabrication, *ACS Applied Energy Materials* 1 (10) (2018) 5268–5279. doi:10.1021/acsaem.8b00885.
- [33] J. Lee, H.-C. Kim, J.-W. Choi, I. H. Lee, A review on 3D printed smart devices for 4D printing, *International Journal of Precision Engineering and Manufacturing-Green Technology* 4 (3) (2017) 373–383. doi:10.1007/s40684-017-0042-x.
- [34] K. R. Ryan, M. P. Down, C. E. Banks, Future of additive manufacturing: Overview of 4D and 3D printed smart and advanced materials and their

- applications, *Chemical Engineering Journal* 403 (2021) 126162. doi:10.1016/j.cej.2020.126162.
- [35] T. J. Wallin, J. Pikul, R. F. Shepherd, 3D printing of soft robotic systems, *Nature Reviews Materials* 3 (6) (2018) 84–100. doi:10.1038/s41578-018-0002-2.
- [36] T. Lu, C. Ma, T. Wang, Mechanics of dielectric elastomer structures: A review, *Extreme Mechanics Letters* 38 (2020) 100752. doi:10.1016/j.eml.2020.100752.
- [37] J. H. Youn, S. M. Jeong, G. Hwang, H. Kim, K. Hyeon, J. Park, K. U. Kyung, Dielectric elastomer actuator for soft robotics applications and challenges, *Applied Sciences (Switzerland)* 10 (2) (2020) 640. doi:10.3390/app10020640.
- [38] I. Kajiwara, S. Kitabatake, N. Hosoya, S. Maeda, Design of dielectric elastomer actuators for vibration control at high frequencies, *International Journal of Mechanical Sciences* 157-158 (2019) 849–857. doi:10.1016/j.ijmecsci.2019.05.019.
- [39] E. Garnell, Dielectric elastomer loudspeakers : models, experiments and optimization, Ph.D. thesis, Institut Polytechnique de Paris (2020).
- [40] X. Ji, X. Liu, V. Cacucciolo, M. Imboden, Y. Civet, A. E. Haitami, S. Cantin, Y. Perriard, H. Shea, An autonomous untethered fast soft robotic insect driven by low-voltage dielectric elastomer actuators, *Science Robotics* 4 (37) (2019). doi:10.1126/SCIROBOTICS.AAZ6451.
- [41] C. Christianson, C. Bayag, G. Li, S. Jadhav, A. Giri, C. Agba, T. Li, M. T. Tolley, Jellyfish-Inspired Soft Robot Driven by Fluid Electrode Dielectric Organic Robotic Actuators, *Frontiers in Robotics and AI* 6 (2019). doi:10.3389/frobt.2019.00126.
- [42] Y. Chen, H. Zhao, J. Mao, P. Chirarattananon, E. F. Helbling, N. s. P. Hyun, D. R. Clarke, R. J. Wood, Controlled flight of a microrobot powered by soft artificial muscles, *Nature* 575 (7782) (2019) 324–329. doi:10.1038/s41586-019-1737-7.
- [43] S. Hau, G. Rizzello, M. Hodgins, A. York, S. Seelecke, Design and control of a high-speed positioning system based on dielectric elastomer

- membrane actuators, *IEEE/ASME Transactions on Mechatronics* 22 (3) (2017) 1259–1267. doi:10.1109/TMECH.2017.2681839.
- [44] M. Ghilardi, H. Boys, P. Török, J. J. C. Busfield, F. Carpi, Smart Lenses with Electrically Tuneable Astigmatism, *Scientific Reports* 2019 9:1 9 (1) (2019) 1–10. doi:10.1038/s41598-019-52168-8.
- [45] X. Ji, X. Liu, V. Cacucciolo, Y. Civet, A. El Haitami, S. Cantin, Y. Perriard, H. Shea, Untethered Feel-Through Haptics Using 18- μ m Thick Dielectric Elastomer Actuators, *Advanced Functional Materials* (2020) 2006639 doi:10.1002/adfm.202006639.
- [46] C. R. Kelley, J. L. Kauffman, Towards wearable tremor suppression using dielectric elastomer stack actuators, *Smart Materials and Structures* 30 (2) (2021) 025006. doi:10.1088/1361-665X/abccdc.
- [47] Q. He, Z. Wang, Y. Wang, A. Minori, M. T. Tolley, S. Cai, Electrically controlled liquid crystal elastomer-based soft tubular actuator with multimodal actuation, *Science Advances* 5 (10) (2019). doi:10.1126/SCIADV.AAX5746.
- [48] C. Cao, X. Gao, A. T. Conn, A Magnetically Coupled Dielectric Elastomer Pump for Soft Robotics, *Advanced Materials Technologies* 4 (8) (2019) 1900128. doi:10.1002/admt.201900128.
- [49] L. J. Romasanta, M. A. Lopez-Manchado, R. Verdejo, Increasing the performance of dielectric elastomer actuators: A review from the materials perspective, *Progress in Polymer Science* 51 (2015) 188–211. doi:10.1016/j.progpolymsci.2015.08.002.
- [50] H. Li, L. Chen, C. Zhao, S. Yang, Evoking or suppressing electromechanical instabilities in soft dielectrics with deformation-dependent dielectric permittivity, *International Journal of Mechanical Sciences* 202-203 (2021) 106507. doi:10.1016/j.ijmecsci.2021.106507.
- [51] M. R. O’Neill, E. Acome, S. Bakarich, S. K. Mitchell, J. Timko, C. Keplinger, R. F. Shepherd, Rapid 3D Printing of Electrohydraulic (HASEL) Tentacle Actuators, *Advanced Functional Materials* 30 (40) (2020) 2005244. doi:10.1002/adfm.202005244.

- [52] W. Zhang, J. Ma, W. Zhang, P. Zhang, W. He, J. Chen, Z. M. Sun, A multidimensional nanostructural design towards electrochemically stable and mechanically strong hydrogel electrodes, *Nanoscale* 12 (12) (2020) 6637–6643. doi:10.1039/d0nr01414a.
- [53] Y. Yang, Q. Huang, G. F. Payne, R. Sun, X. Wang, A highly conductive, pliable and foldable Cu/cellulose paper electrode enabled by controlled deposition of copper nanoparticles, *Nanoscale* 11 (2) (2019) 725–732. doi:10.1039/c8nr07123c.
- [54] H. Wu, W. P. Fahy, S. Kim, H. Kim, N. Zhao, L. Pilato, A. Kafi, S. Bateman, J. H. Koo, Recent developments in polymers/polymer nanocomposites for additive manufacturing, *Progress in Materials Science* 111 (2020) 100638. doi:10.1016/j.pmatsci.2020.100638.
- [55] A. Bele, C. Tugui, M. Asandulesa, D. Ionita, L. Vasiliu, G. Stiubianu, M. Iacob, C. Racles, M. Cazacu, Conductive stretchable composites properly engineered to develop highly compliant electrodes for dielectric elastomer actuators, *Smart Materials and Structures* 27 (10) (2018) 105005. doi:10.1088/1361-665X/aad977.
- [56] K. Yu, A. Xin, H. Du, Y. Li, Q. Wang, Additive manufacturing of self-healing elastomers, *NPG Asia Materials* 2019 11:1 11 (1) (2019) 1–11. doi:10.1038/s41427-019-0109-y.
- [57] S. J. Dünki, Y. S. Ko, F. A. Nüesch, D. M. Opris, Self-Repairable, High Permittivity Dielectric Elastomers with Large Actuation Strains at Low Electric Fields, *Advanced Functional Materials* 25 (16) (2015) 2467–2475. doi:10.1002/ADFM.201500077.
- [58] A. Goshkoderia, N. Arora, V. Slesarenko, J. Li, V. Chen, A. Juhl, P. Buskohl, S. Rudykh, Tunable permittivity in dielectric elastomer composites under finite strains: Periodicity, randomness, and instabilities., *International Journal of Mechanical Sciences* 186 (2020) 105880. doi:10.1016/j.ijmecsci.2020.105880.
- [59] D. M. Opris, Polar Elastomers as Novel Materials for Electromechanical Actuator Applications, *Advanced Materials* 30 (5) (2018) 1703678. doi:10.1002/ADMA.201703678.

- [60] Z. Li, M. Sheng, M. Wang, P. Dong, B. Li, H. Chen, Stacked dielectric elastomer actuator (SDEA): Casting process, modeling and active vibration isolation, *Smart Materials and Structures* 27 (7) (2018) 075023. doi:10.1088/1361-665X/aabea5.
- [61] J. Rossiter, P. Walters, B. Stoimenov, Printing 3D dielectric elastomer actuators for soft robotics, in: Y. Bar-Cohen, T. Wallmersperger (Eds.), *Electroactive Polymer Actuators and Devices (EAPAD) 2009*, Vol. 7287, 2009, p. 72870H. doi:10.1117/12.815746.
- [62] G. Haghiashtiani, E. Habtour, S.-H. Park, F. Gardea, M. C. McAlpine, 3D printed electrically-driven soft actuators, *Extreme Mechanics Letters* 21 (2018) 1–8. doi:10.1016/j.eml.2018.02.002.
- [63] A. Chortos, E. Hajiesmaili, J. Morales, D. R. Clarke, J. A. Lewis, 3D Printing of Interdigitated Dielectric Elastomer Actuators, *Advanced Functional Materials* 30 (1) (2020) 1907375. doi:10.1002/adfm.201907375.
- [64] D. Gonzalez, J. Garcia, B. Newell, Electromechanical characterization of a 3D printed dielectric material for dielectric electroactive polymer actuators, *Sensors and Actuators, A: Physical* 297 (2019) 111565. doi:10.1016/j.sna.2019.111565.
- [65] B. Shaqour, M. Abuabiah, S. Abdel-Fattah, A. Juaidi, R. Abdallah, W. Abuzaina, M. Qarout, B. Verleije, P. Cos, Gaining a better understanding of the extrusion process in fused filament fabrication 3D printing: a review, *The International Journal of Advanced Manufacturing Technology* 114 (5-6) (2021) 1279–1291. doi:10.1007/s00170-021-06918-6.
- [66] S. Singh, G. Singh, C. Prakash, S. Ramakrishna, Current status and future directions of fused filament fabrication, *Journal of Manufacturing Processes* 55 (2020) 288–306. doi:10.1016/j.jmapro.2020.04.049.
- [67] D. Fico, D. Rizzo, R. Casciaro, C. Esposito Corcione, A Review of Polymer-Based Materials for Fused Filament Fabrication (FFF): Focus on Sustainability and Recycled Materials, *Polymers* 14 (3) (2022) 465. doi:10.3390/polym14030465.

- [68] P. M. Angelopoulos, M. Samouhos, M. Taxiarchou, Functional fillers in composite filaments for fused filament fabrication; a review, *Materials Today: Proceedings* 37 (2021) 4031–4043. doi:10.1016/j.matpr.2020.07.069.
- [69] A. García-Collado, J. M. Blanco, M. K. Gupta, R. Dorado-Vicente, Advances in polymers based Multi-Material Additive-Manufacturing Techniques: State-of-art review on properties and applications, *Additive Manufacturing* 50 (2022) 102577. doi:10.1016/J.ADDMA.2021.102577.
- [70] R. Pelrine, R. Kornbluh, Q. Pei, J. Joseph, High-speed electrically actuated elastomers with strain greater than 100%, *Science* 287 (5454) (2000) 836–839. doi:10.1126/science.287.5454.836.
- [71] F. Carpi, I. Anderson, S. Bauer, G. Frediani, G. Gallone, M. Gei, C. Graaf, C. Jean-Mistral, W. Kaal, G. Kofod, M. Kollosche, R. Kornbluh, B. Lassen, M. Matysek, S. Michel, S. Nowak, B. O’Brien, Q. Pei, R. Pelrine, B. Rechenbach, S. Rosset, H. Shea, Standards for dielectric elastomer transducers, *Smart Materials and Structures* 24 (10) (2015) 105025. doi:10.1088/0964-1726/24/10/105025.
- [72] M. Aurilia, F. Piscitelli, L. Sorrentino, M. Lavorgna, S. Iannace, Detailed analysis of dynamic mechanical properties of TPU nanocomposite: The role of the interfaces, *European Polymer Journal* 47 (5) (2011) 925–936. doi:10.1016/j.eurpolymj.2011.01.005.
- [73] P. Brochu, Q. Pei, Advances in dielectric elastomers for actuators and artificial muscles, *Macromolecular Rapid Communications* 31 (1) (2010) 10–36. doi:10.1002/MARC.200900425.
- [74] Y. Zhao, Q. Guo, S. Wu, G. Meng, W. Zhang, Design and experimental validation of an annular dielectric elastomer actuator for active vibration isolation, *Mechanical Systems and Signal Processing* 134 (2019) 106367. doi:10.1016/j.ymsp.2019.106367.
- [75] Z. Wang, B. He, Y. Zhou, R. Shen, G. Li, Effects of pre-stretch on the oscillation and stability of dielectric elastomers, *International Journal of Mechanical Sciences* 185 (2020) 105879. doi:10.1016/j.ijmecsci.2020.105879.

- [76] J. Maas, D. Tepel, T. Hoffstadt, Actuator design and automated manufacturing process for DEAP-based multilayer stack-actuators, *Meccanica* 50 (11) (2015) 2839–2854. doi:10.1007/s11012-015-0273-2.
- [77] P. Awasthi, S. S. Banerjee, Fused deposition modeling of thermoplastic elastomeric materials: Challenges and opportunities, *Additive Manufacturing* 46 (2021) 102177. doi:10.1016/J.ADDMA.2021.102177.
- [78] X. He, J. Zhou, L. Jin, X. Long, H. Wu, L. Xu, Y. Gong, W. Zhou, Improved dielectric properties of thermoplastic polyurethane elastomer filled with core-shell structured PDA@TiC particles, *Materials* 13 (15) (2020) 3341. doi:10.3390/ma13153341.
- [79] J. Wei, L. Zhu, Intrinsic polymer dielectrics for high energy density and low loss electric energy storage, *Progress in Polymer Science* 106 (2020) 101254. doi:10.1016/J.PROGPOLYMSCI.2020.101254.
- [80] D. J. Roach, C. M. Hamel, C. K. Dunn, M. V. Johnson, X. Kuang, H. J. Qi, The m4 3D printer: A multi-material multi-method additive manufacturing platform for future 3D printed structures, *Additive Manufacturing* 29 (2019) 100819. doi:10.1016/j.addma.2019.100819.
- [81] Y. Hu, Recent progress in field-assisted additive manufacturing: materials, methodologies, and applications, *Materials Horizons* 8 (3) (2021) 885–911. doi:10.1039/D0MH01322F.